Electronic Supplementary Information

Halogen bonding to the azulene π-system: cocrystal design of pleochroism

Jogirdas Vainauskas, Filip Topić, Oleksandr S. Bushuyev, Christopher J. Barrett* and Tomislav Friščić*

Table of Contents

1. Experimental details

All solvents used for syntheses and crystal growth were of reagent grade and were used as received. Azulene (**azu**) was purchased from Alfa Aesar, and 1,2,4,5-tetrafluoro-3,6-diiodobenzene (**14tfib**) was purchased from Oakwood Products, Inc. The compound *trans*-2,3,5,6,2',3',5',6'-octafluoro-4,4'-diiodoazobenzene (**ofiab**) was synthesized as described previously.[1]

Mechanochemical experiments were conducted on an FTS-1000 shaker mill using a pair of 14 mL stainless steel milling jars with two stainless steel balls each (0.7 g weight). In a typical experiment, co-formers were added to a milling jar in the desired stoichiometric ratio with a total mass of 200 mg, along with 50 µL of nitromethane and the steel balls and were ground for 20 min at a frequency of 1800 rpm/30 Hz.

Powder X-ray diffraction (PXRD) experiments were performed on a Bruker D2 Phaser diffractometer using nickel-filtered CuK_α radiation (λ = 1.54184 Å) from a source operating at 10 mA and 30 kV and equipped with a Lynxeye linear position sensitive detector, in the 2θ range of 4–40°, step size of 0.049° and measuring time of 1 s per step.

Attenuated total reflectance Fourier-transform infrared (ATR-FTIR) spectra were measured on a Bruker VERTEX 70 instrument equipped with a single-reflection diamond crystal Platinum ATR unit.

Thermal analysis, *i.e.* simultaneous TGA and DSC measurements were performed using a Mettler-Toledo TGA/DSC 1 Thermal Analyzer in open alumina crucibles (70 µL volume), heated in a stream of nitrogen (50 mL min^{-1}) from 30 to 250 °C at a heating rate of 20 (**azu** and **14tfib**) or 10 °C min^{-1} [(**azu**)$_2$(**14tfib**)$_3$, (**azu**)(**14tfib**)$_2$ and (**nap**)(**14tfib**)$_2$]. Data collection and analysis were performed using the STAR^e Software 16.20 program package.[2]

2. Mechanochemical cocrystal screening

A series of mixtures of **azu** or **nap** and **14tfib** was prepared, in 2:1, 1:1, 2:3 or 1:2 stoichiometric ratios, respectively, with total mass of 200 mg. Each mixture was placed in a stainless-steel jar along with two 0.7 g stainless steel balls and 50 uL of nitromethane, and subsequently milled for 20 min at 1800 rpm/30 Hz, using a Form-Tech Scientific FTS1000 shaker mill.

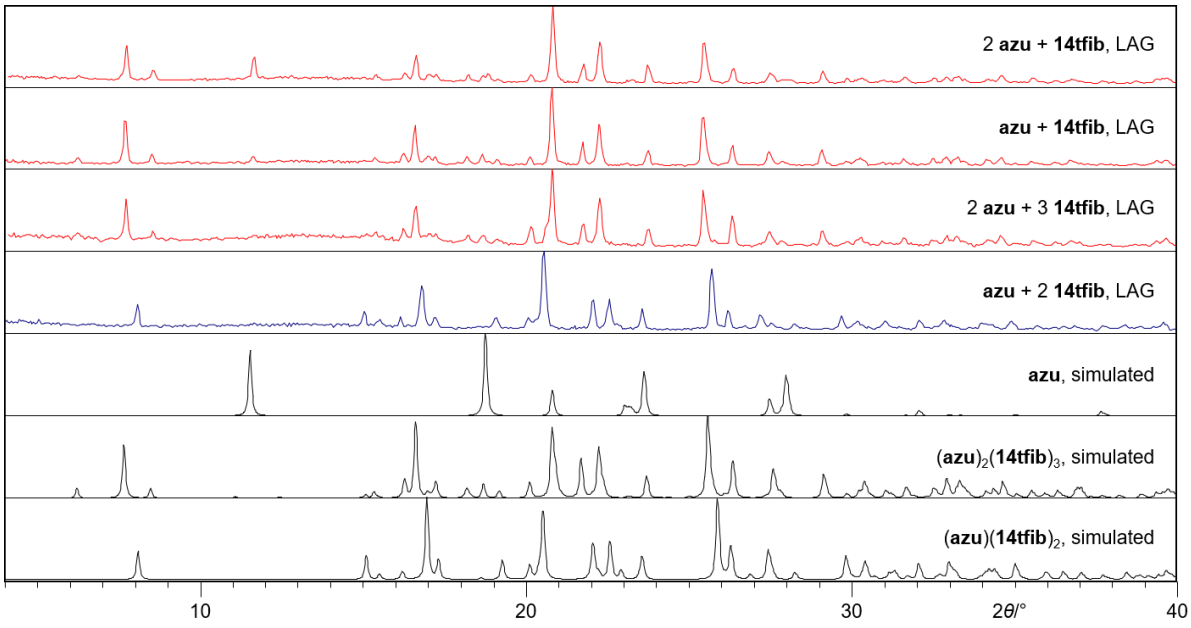

Figure S1. Comparison of selected PXRD patterns of mechanochemically prepared reaction mixtures of **azu** and **14tfib** with the simulated patterns for the solid reactant **azu** (CSD AZLENE) and the here reported crystal structures of (**azu**)$_2$(**14tfib**)$_3$ and (**azu**)(**14tfib**)$_2$. The PXRD patterns reveal the formation of the cocrystal (**azu**)(**14tfib**)$_2$ in case of the 1:2 **azu** : **14tfib** stoichiometry, and (**azu**)(**14tfib**)$_2$ alone or as a mixture with **azu** for other stoichiometries (2:3, 1:1, 2:1).

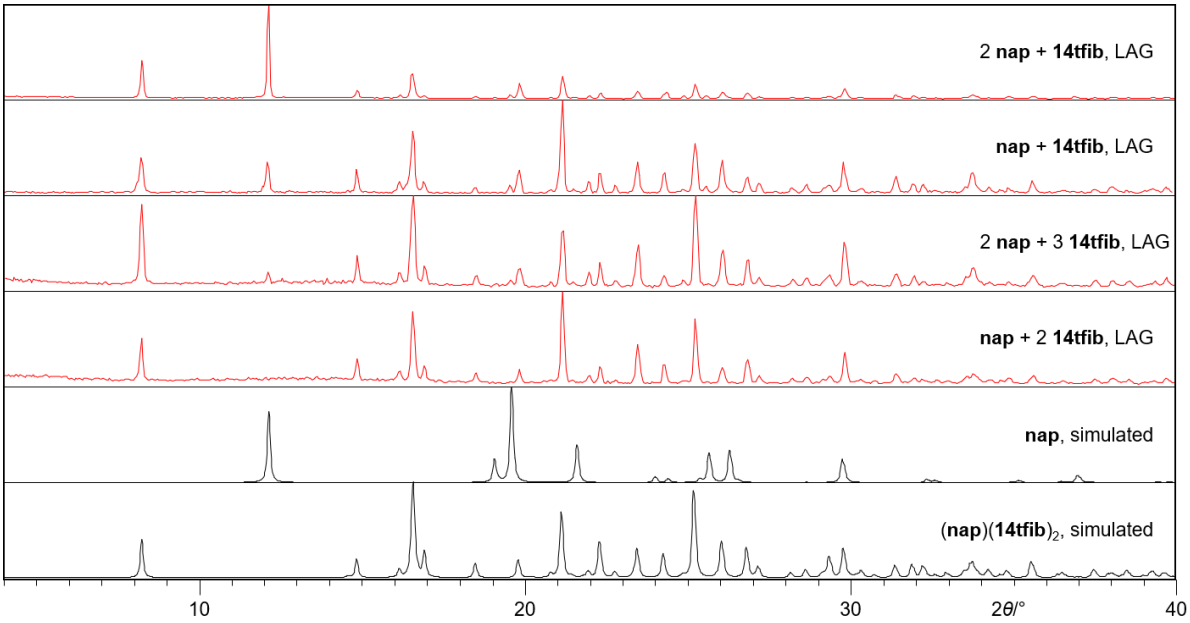

Figure S2. Comparison of selected PXRD patterns of mechanochemically prepared reaction mixtures of **nap** and **14tfib** with the simulated patterns for the solid reactant **nap** (CSD NAPHTA36) and the known crystal structure of (**nap**)(**14tfib**)$_2$ (CSD NICTAW). The PXRD patterns reveal the formation of the cocrystal (**nap**)(**14tfib**)$_2$ in all cases.

3. Single crystal growth

Single crystals of (**azu**)$_2$(**14tfib**)$_3$ were obtained by recrystallization of a sample obtained by LAG from hexanes.

Single crystals of (**azu**)(**14tfib**)$_2$ were obtained by recrystallization of a sample obtained by LAG from acetone.

Single crystals of (**azu**)(**ofiab**)$_2$ obtained by crystallization of a few milligrams of a mixture of **azu** and **ofiab** in 1:2 ratio from dichloromethane.

Single crystals of (**azu**)$_3$(**ofiab**)$_2$ were obtained by crystallization of a few milligrams of a mixture of **azu** and **ofiab** in 3:2 ratio from chloroform.

4. Crystal structure determinations

The X-ray data for (**azu**)$_2$(**14tfib**)$_3$@253K, (**azu**)(**14tfib**)$_2$, and (**azu**)$_3$(**ofiab**)$_2$ were collected on a Bruker D8 Venture dual-source diffractometer equipped with a PHOTON II detector and an Oxford Cryostream 800 cooling system, using mirror-monochromated Cu*K*α radiation (λ = 1.54184 Å) from a microfocus source. The X-ray data for (**azu**)$_2$(**14tfib**)$_3$@150K and (**azu**)(**ofiab**)$_2$ were collected on a Bruker SMART diffractometer equipped with an APEX II detector and an Oxford Cryostream cooling system, using graphite-monochromated Mo*K*α radiation (λ = 0.71073 Å) from a fine-focus source. Data were collected in a series of φ- and ω-scans. APEX3 software was used for data collection, integration and reduction.[3] Numerical absorption corrections were applied using SADABS-2016/2.[4]

Structures were solved by dual-space iterative methods using SHELXT[5] and refined by full-matrix least-squares on F^2 using all data with SHELXL[6] within the OLEX2[7] and/or WinGX[8] environment. In all cases, some reflections were found to have been obscured by the beam stop and were omitted from the refinement. Extinction correction was applied in case of (**azu**)$_2$(**14tfib**)$_3$@253K, (**azu**)(**14tfib**)$_2$, and (**azu**)(**ofiab**)$_2$. Hydrogen atoms were placed in calculated positions and treated as riding on the parent carbon atoms with isotropic displacement parameters 1.2 times larger than the respective parent atoms. Geometrical restraints for 1,2- and 1,3-distances in **azu** were derived from the structure of (**azu**)$_2$(**14tfib**)$_3$@150K and applied to all other structures. Moreover, planarity restrains were applied to **azu** in the structures of (**azu**)(**14tfib**)$_2$, (**azu**)(**ofiab**)$_2$ and (**azu**)$_3$(**ofiab**)$_2$. Rigid bond and proximity restraints were applied to the anisotropic displacement parameters (ADPs) of all the atoms belonging to disordered moieties.

In the structures of (**azu**)(**14tfib**)$_2$, (**azu**)(**ofiab**)$_2$ and (**azu**)$_3$(**ofiab**)$_2$, **azu** was found to exhibit the well-known two-component disorder around inversion centre and was modelled with half-occupancy. In addition to that, in the structure of (**azu**)$_3$(**ofiab**)$_2$, another molecule of **azu** was modelled as disordered over two components with their occupancies refined freely with the sum fixed to 100 %.

In (**azu**)(**ofiab**)$_2$ and (**azu**)$_3$(**ofiab**)$_2$, **ofiab** was modelled as disordered over two components with their occupancies refined freely with the sum fixed to 100 %. However, the occupancies of the minor components refined to 7.4(3) % and 5.6(5) %, respectively, for (**azu**)(**ofiab**)$_2$ and (**azu**)$_3$(**ofiab**)$_2$. Because of that, minor components were initially refined with hard restraints applied to the geometry and ADPs to establish a reasonable geometry for these moieties. Due to very low occupancies, restrained refinement was considered not physically sensible, and the constrained refinement was used subsequently, with (only) the minor disorder components refined as rigid bodies and the ADPs of all of their atoms constrained to be equal to the closest appropriate atoms of the major disorder component.

Crystal structure figures were generated using Mercury[9] and POV-Ray.[10]

CCDC 2000772–2000775 and 2004308 contain the supplementary crystallographic data for this paper. The data can be obtained free of charge from The Cambridge Crystallographic Data Centre via www.ccdc.cam.ac.uk/structures.

Table S1. Crystallographic data for all the crystal structures reported in this work (**azu**)$_2$(**14tfib**)$_3$, (**azu**)(**14tfib**)$_2$, (**azu**)(**ofiab**)$_2$ and (**azu**)$_3$(**ofiab**)$_2$.

Compound	(**azu**)$_2$(**14tfib**)$_3$	(**azu**)$_2$(**14tfib**)$_3$	(**azu**)(**14tfib**)$_2$	(**azu**)(**ofiab**)$_2$	(**azu**)$_3$(**ofiab**)$_2$
CCDC code	2000772	2004308	2000773	2000774	2000775
T (K)	150.0(1)	253.0(1)	253.0(1)	150.0(1)	253.0(1)
Formula	$C_{38}H_{16}F_{12}I_6$	$C_{38}H_{16}F_{12}I_6$	$C_{22}H_8F_8I_4$	$C_{34}H_8F_{16}I_4N_4$	$C_{54}H_{24}F_{16}I_4N_4$
M_r	1461.91	1461.91	931.88	1284.04	1540.37
Crystal system	triclinic	triclinic	triclinic	triclinic	triclinic
Space group	$P\bar{1}$	$P\bar{1}$	$P\bar{1}$	$P\bar{1}$	$P\bar{1}$
a (Å)	5.9321(6)	5.9617(2)	5.9541(4)	6.0619(9)	6.0053(3)
b (Å)	11.9878(13)	12.0425(4)	9.6644(7)	11.9613(17)	11.9473(5)
c (Å)	14.8586(16)	14.9758(5)	11.8639(9)	12.6449(18)	18.8788(7)
α (°)	73.9545(12)	73.9375(13)	67.331(2)	88.7995(16)	71.556(4)
β (°)	80.1893(13)	80.8173(15)	85.205(3)	79.8911(17)	89.199(3)
γ (°)	84.8797(12)	85.0271(16)	80.816(2)	88.7903(17)	83.434(4)
V (Å^3)	999.63(18)	1018.93(6)	621.68(8)	902.3(2)	1276.14(10)
Z	1	1	1	1	1
ρ_{calc} (g cm^{-3})	2.428	2.382	2.489	2.363	2.004
μ (mm^{-1})	4.746	36.666	5.081	3.571	20.086
F(000)	670	670	424	596	732
Crystal size (mm^3)	0.534×0.173×0.050	0.942×0.329×0.098	0.185×0.159×0.089	0.660×0.164×0.104	0.173×0.076×0.030
Data collection θ range (°)	1.443–28.861	3.102–72.728	2.306–31.199	1.636–28.968	2.468–79.776
Reflections collected [R_{int}]	9931 [0.0191]	14753 [0.0632]	11276 [0.0270]	11017 [0.0284]	15831 [0.0515]
Reflections [$I > 2\sigma(I)$]	4740 [3970]	3942 [3210]	4012 [2646]	4351 [3476]	5150 [3616]
Data completeness (%)	99.5 to θ = 25.25°	99.5 to θ = 67.75°	99.3 to θ = 25.25°	99.8 to θ = 25.25°	97.0 to θ = 67.75°
Data/restraints/parameters	4740/34/253	3942/34/254	4012/182/200	4351/1411/375	5150/2126/507
Goodness-of-fit on F^2	1.021	1.038	1.023	1.028	1.024
Final R, data with $I > 2\sigma(I)$	R_1 = 0.0251 wR_2 = 0.0595	R_1 = 0.0719 wR_2 = 0.2037	R_1 = 0.0391 wR_2 = 0.0670	R_1 = 0.0285 wR_2 = 0.0666	R_1 = 0.0457 wR_2 = 0.1107
Final R for all data	R_1 = 0.0328 wR_2 = 0.0637	R_1 = 0.0818 wR_2 = 0.2292	R_1 = 0.0708 wR_2 = 0.0774	R_1 = 0.0394 wR_2 = 0.0722	R_1 = 0.0677 wR_2 = 0.1346
Largest diff. peak/hole (e Å^{-3})	0.894/−1.083	1.582/−2.329	1.421/−1.473	0.961/−0.758	1.180/−1.038
Extinction coefficient	-	0.0071(7)	0.0062(9)	0.0016(3)	-

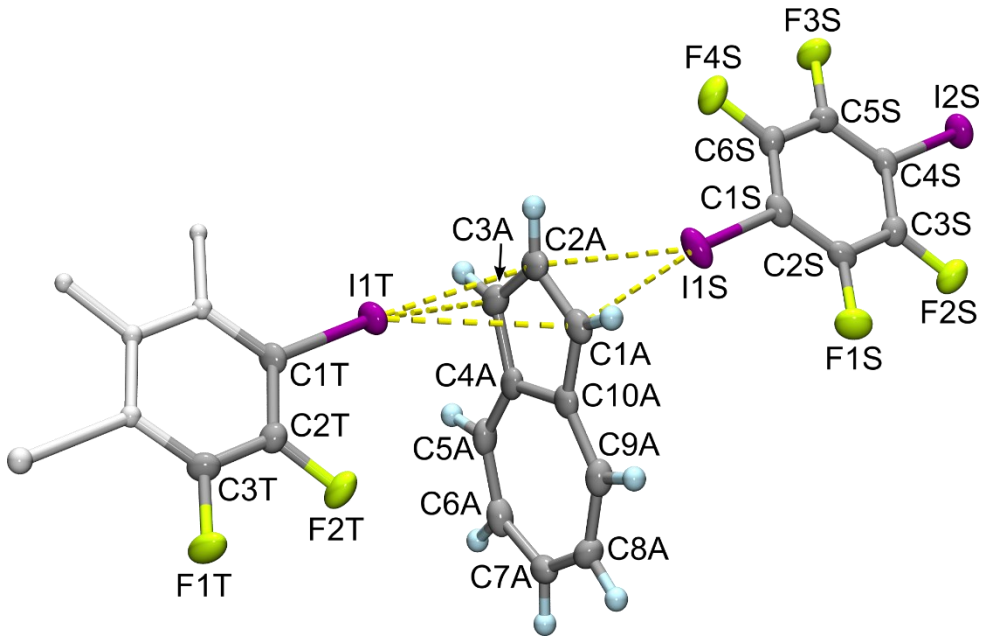

Figure S3. Asymmetric unit of (**azu**)$_2$(**14tfib**)$_3$, collected at 150 K, showing the atom labelling scheme. Displacement ellipsoids are drawn at the 50 % probability level and the hydrogen atoms are shown as small spheres of arbitrary radius. The symmetry-dependent part of one of the **14tfib** molecules is shown in ball-and-stick model in light grey. Halogen bonds are shown as dashed yellow lines.

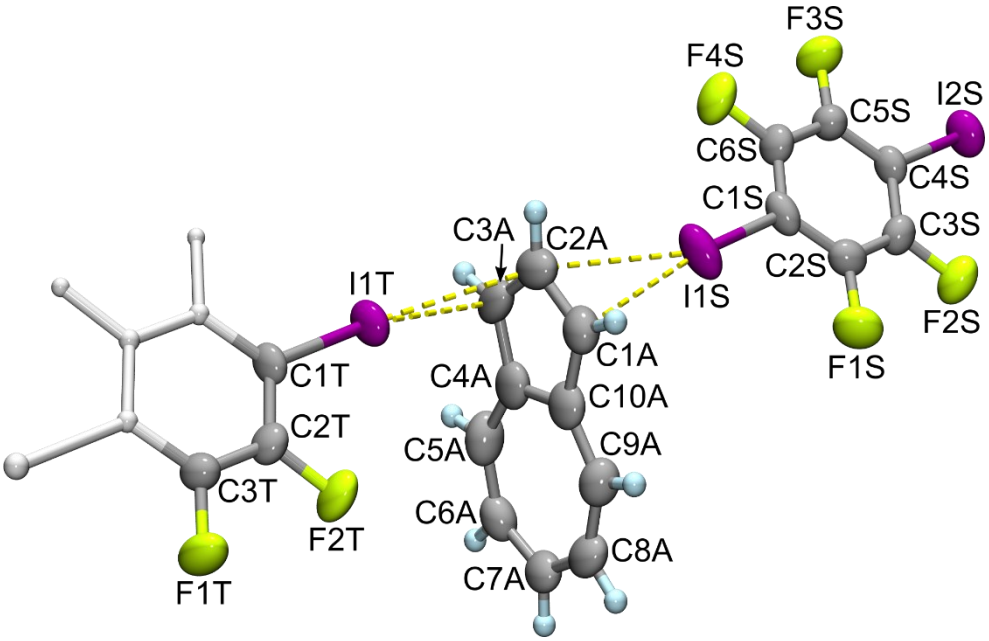

Figure S4. Asymmetric unit of (**azu**)$_2$(**14tfib**)$_3$, collected at 253 K, showing the atom labelling scheme. Displacement ellipsoids are drawn at the 50 % probability level and the hydrogen atoms are shown as small spheres of arbitrary radius. The symmetry-dependent part of one of the **14tfib** molecules is shown in ball-and-stick model in light grey. Halogen bonds are shown as dashed yellow lines.

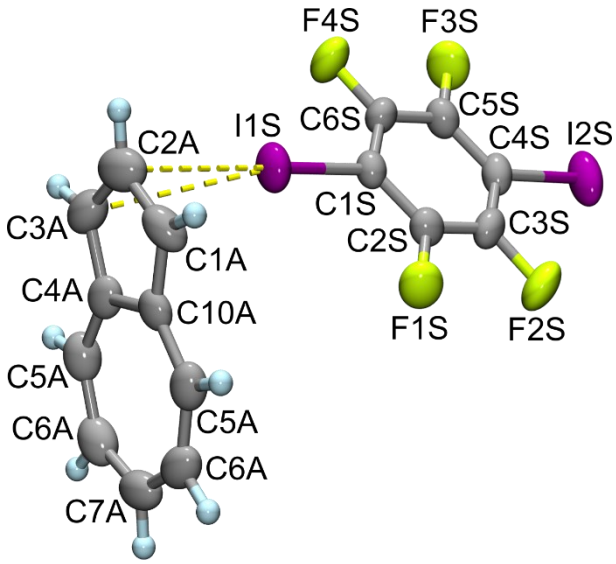

Figure S5. Asymmetric unit of (**azu**)(**14tfib**)$_2$, collected at 253 K, showing the atom labelling scheme. Displacement ellipsoids are drawn at the 50 % probability level and the hydrogen atoms are shown as small spheres of arbitrary radius. Halogen bonds are shown as dashed yellow lines.

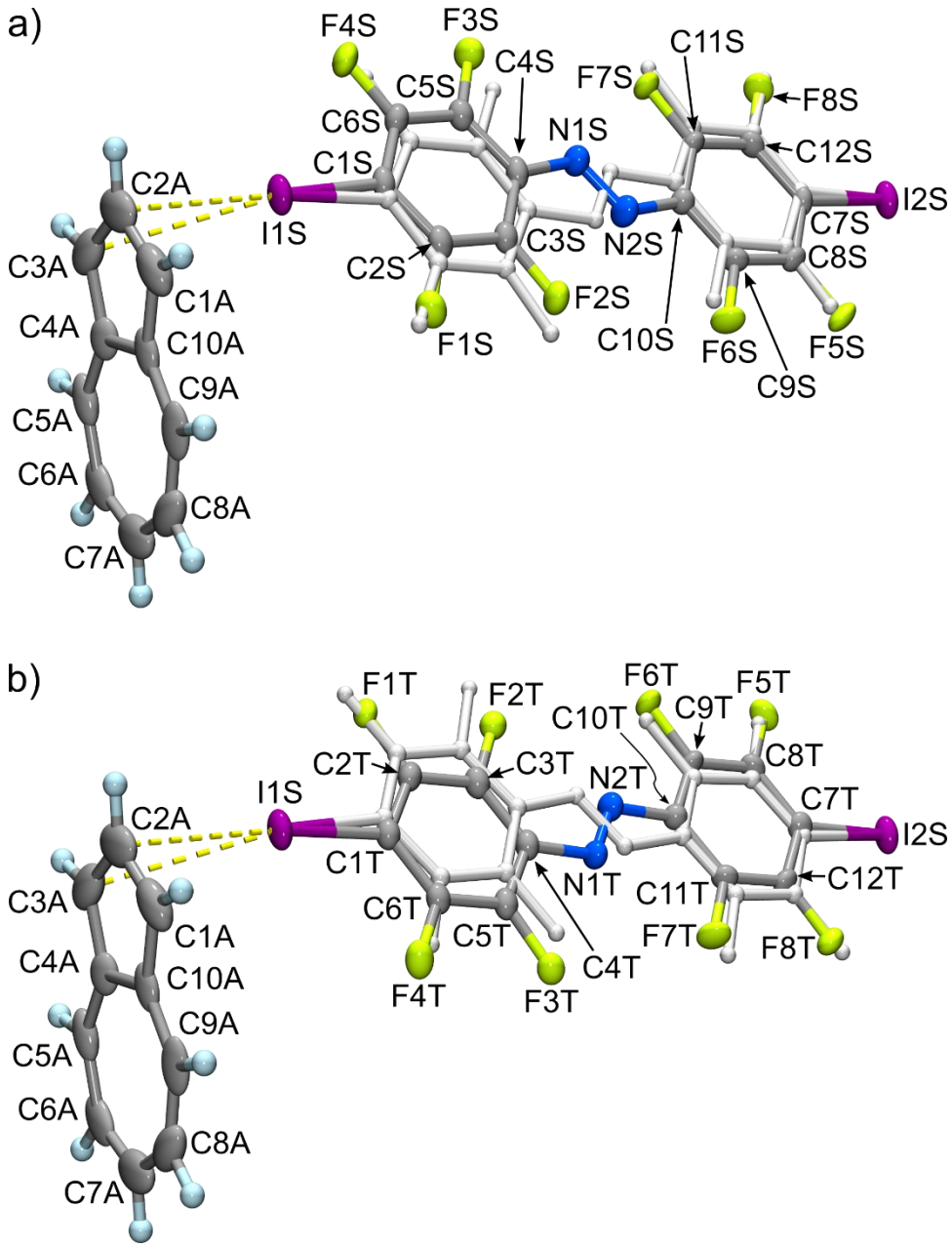

Figure S6. Asymmetric unit of (**azu**)(**ofiab**)$_2$, collected at 150 K, showing the atom labelling scheme. Major and minor disorder components of **ofiab** are highlighted and labelled in a) and b), respectively, with the other component shown in ball-and-stick model and in light grey. Displacement ellipsoids are drawn at the 50 % probability level and the hydrogen atoms are shown as small spheres of arbitrary radius. Halogen bonds are shown as dashed yellow lines.

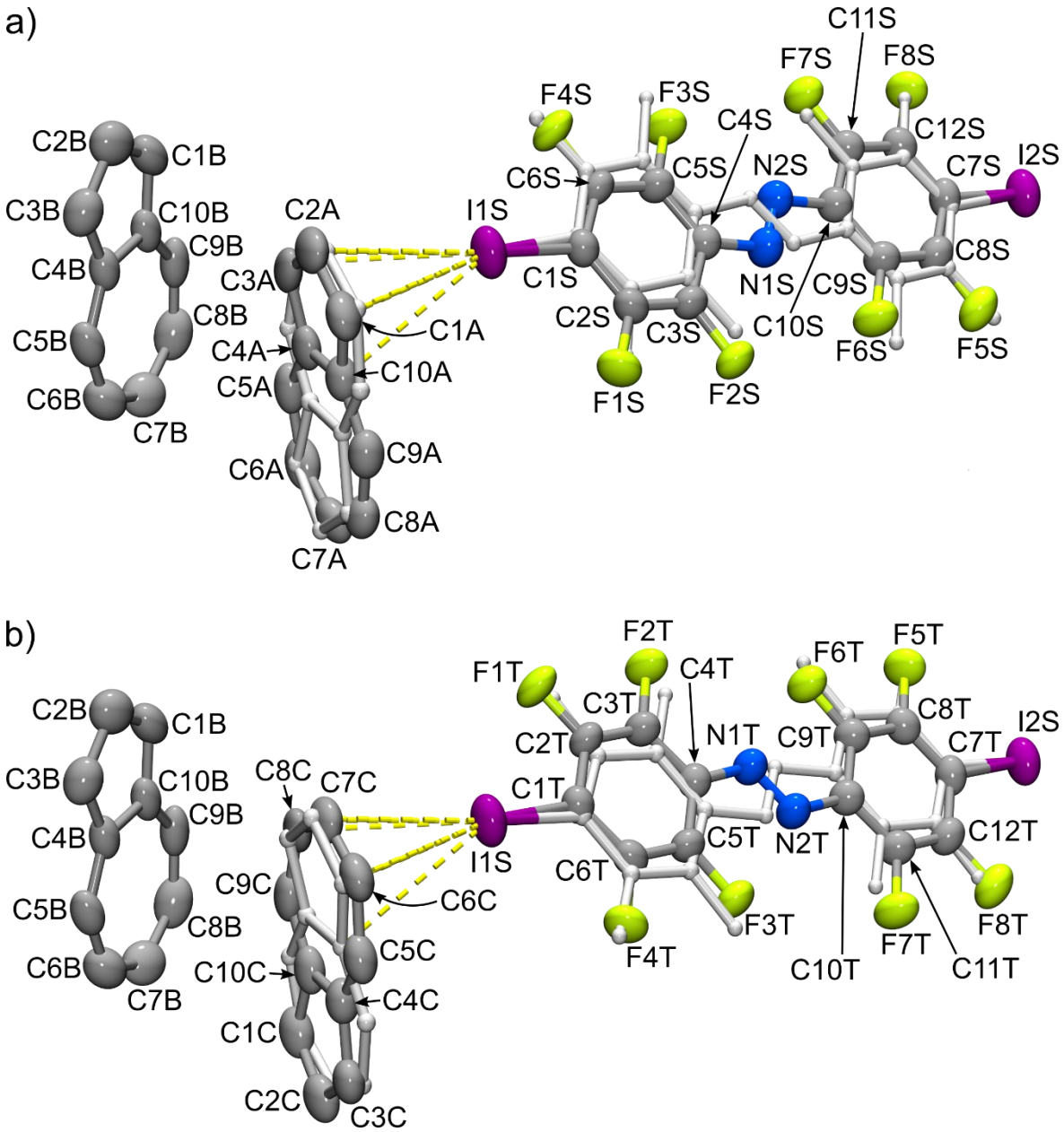

Figure S7. Asymmetric unit of (**azu**)$_3$(**ofiab**)$_2$, collected at 253 K, showing the atom labelling scheme. Displacement ellipsoids are drawn at the 50 % probability level. Major and minor disorder components of **azu** and **ofiab** are highlighted and labelled in a) and b), respectively, with the other component shown in ball-and-stick model and in light grey. Displacement ellipsoids are drawn at the 50 % probability level and the hydrogen atoms are omitted for clarity. Halogen bonds are shown as dashed yellow lines.

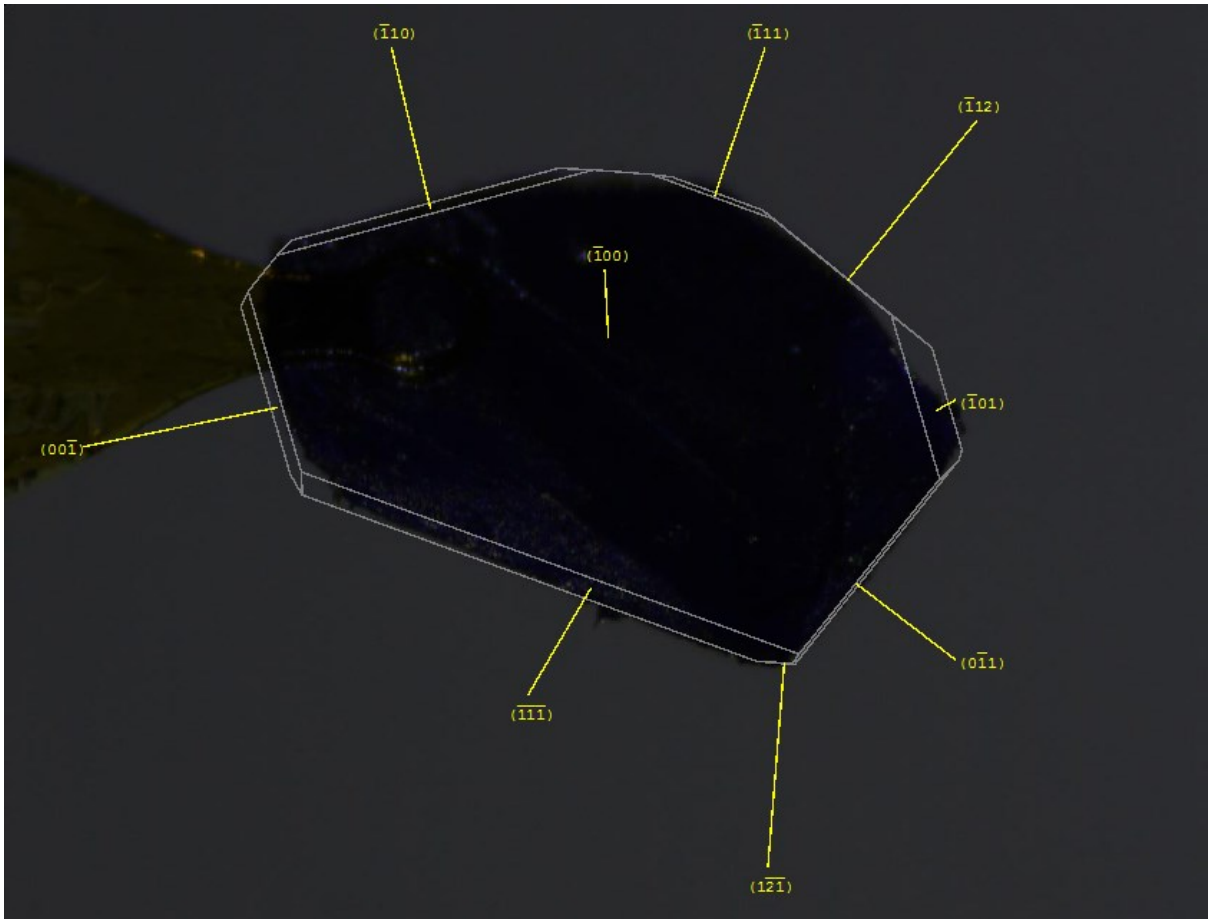

Figure S8. Crystal of **azu** with most pronounced crystal faces indexed.

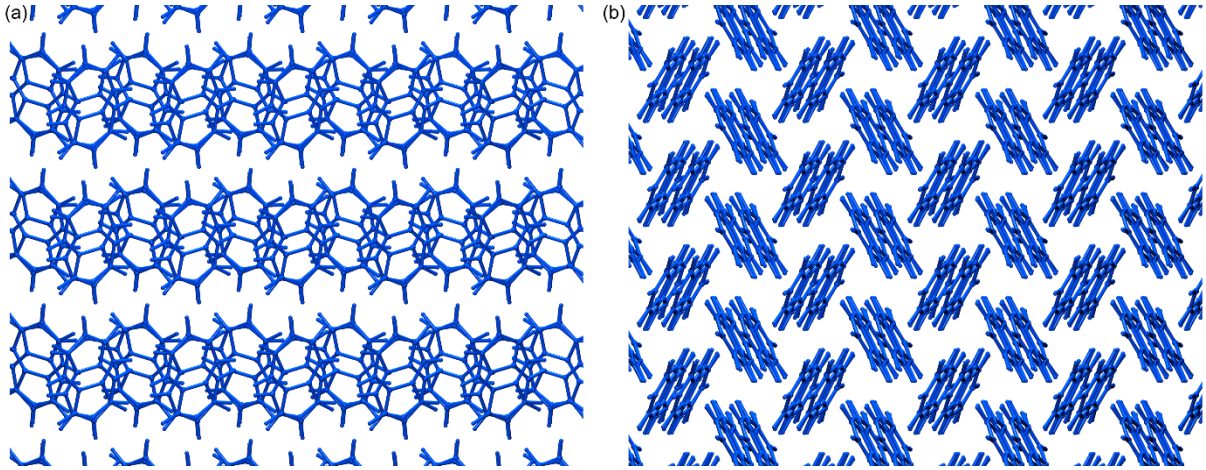

Figure S9. Two views of the crystal structure of **azu** perpendicular to the crystallographic planes (a) (100) and (b) (001).

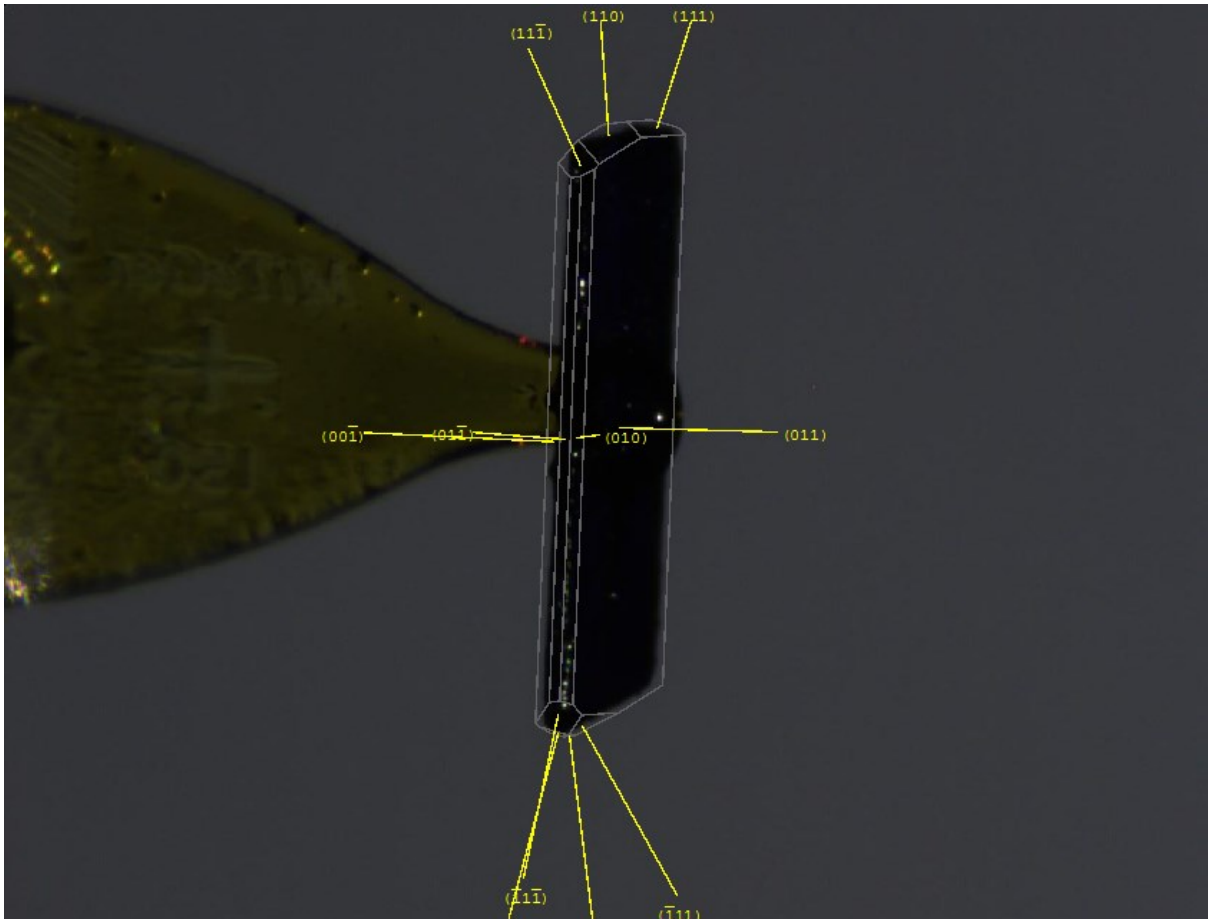

Figure S10. Crystal of (**azu**)$_2$(**14tfib**)$_3$ with most pronounced crystal faces indexed.

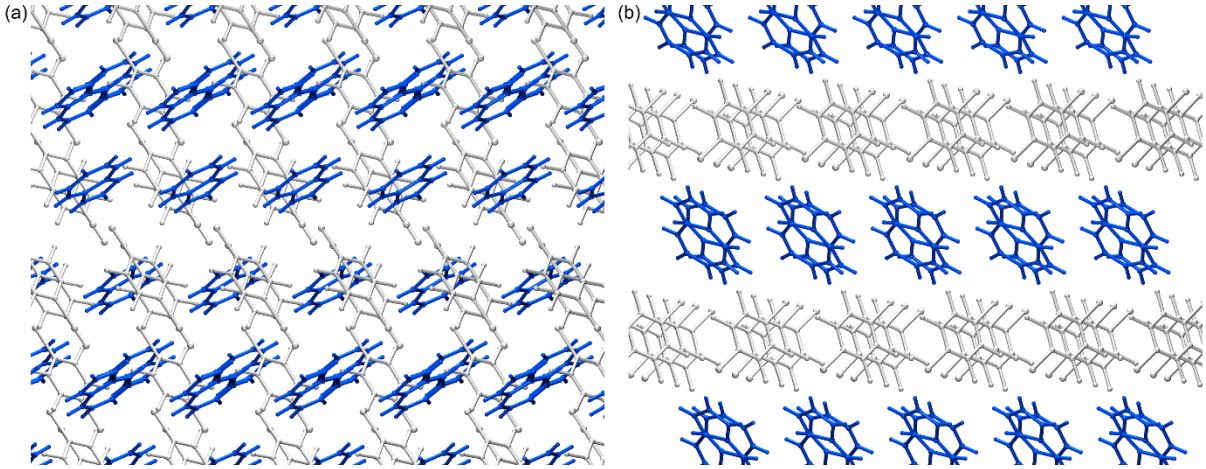

Figure S11. Two views of the crystal structure of (**azu**)$_2$(**14tfib**)$_3$ perpendicular to the crystallographic planes (a) (011) and (b) (001). Note the parallel alignment of **azu** groups.

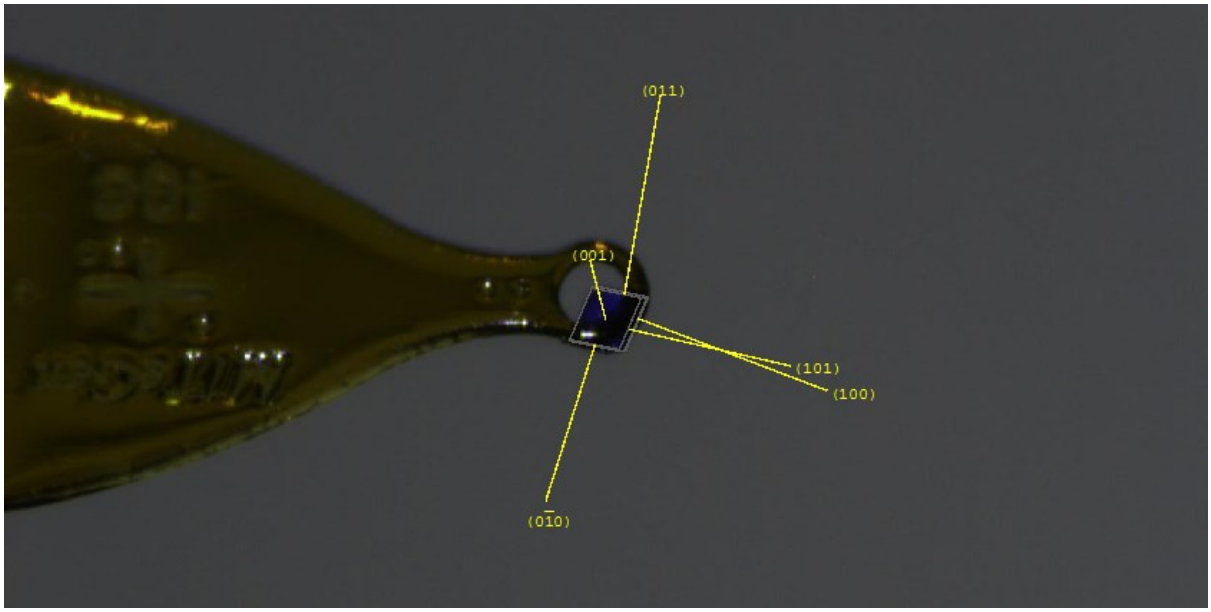

Figure S12. Crystal of (**azu**)(**14tfib**)$_2$ with most pronounced crystal faces indexed.

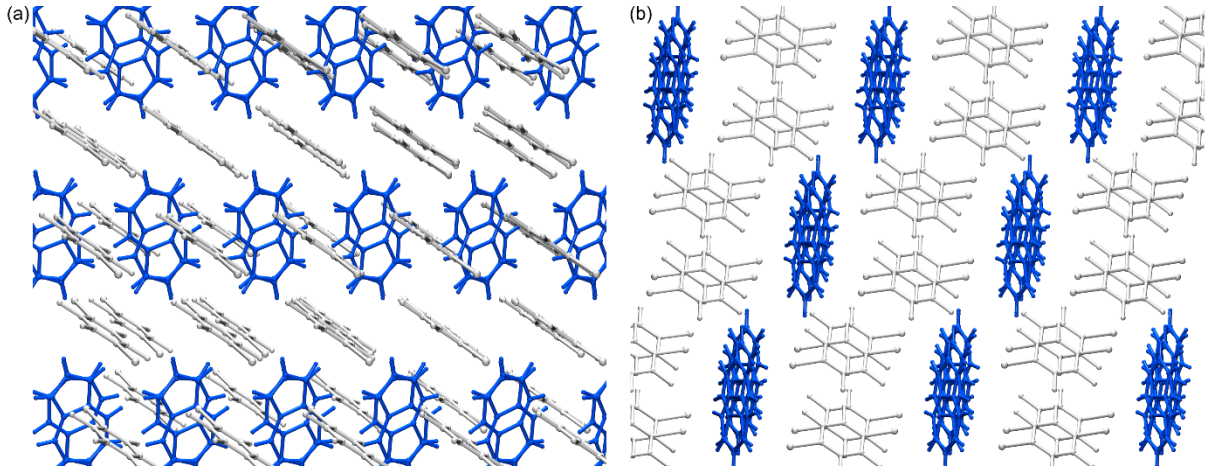

Figure S13. Two views of the crystal structure of (**azu**)(**14tfib**)$_2$ perpendicular to the crystallographic planes (a) (001) and (b) (100). Note the parallel alignment of **azu** groups.

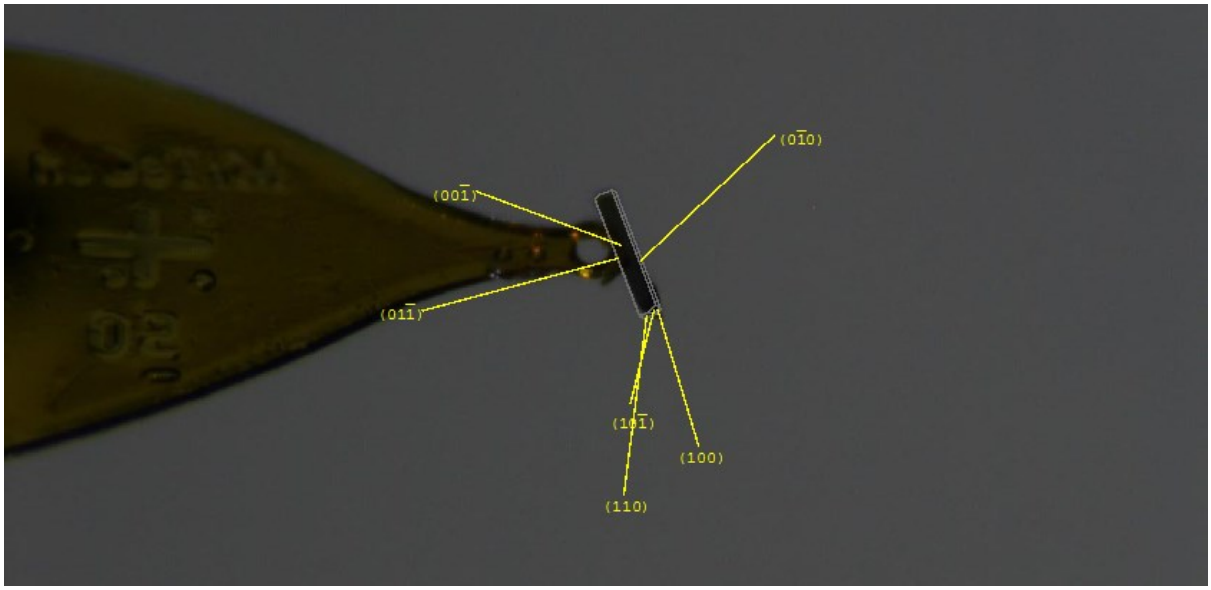

Figure S14. Crystal of (**azu**)(**ofiab**)$_2$ with most pronounced crystal faces indexed.

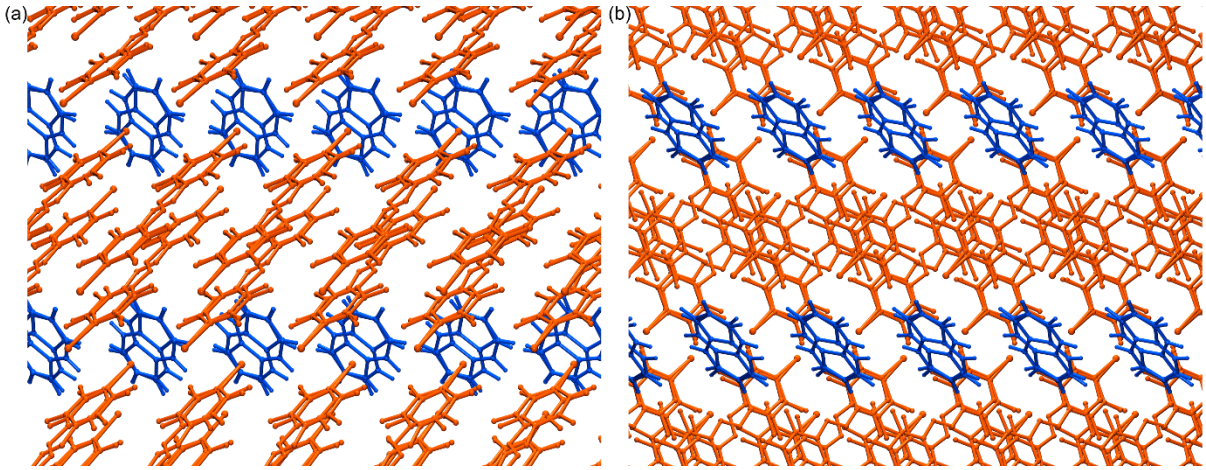

Figure S15. Two views of the crystal structure of (**azu**)(**ofiab**)$_2$ perpendicular to the crystallographic planes (a) (001) and (b) (010). Note the parallel alignment of **azu** groups and of **ofiab** moieties.

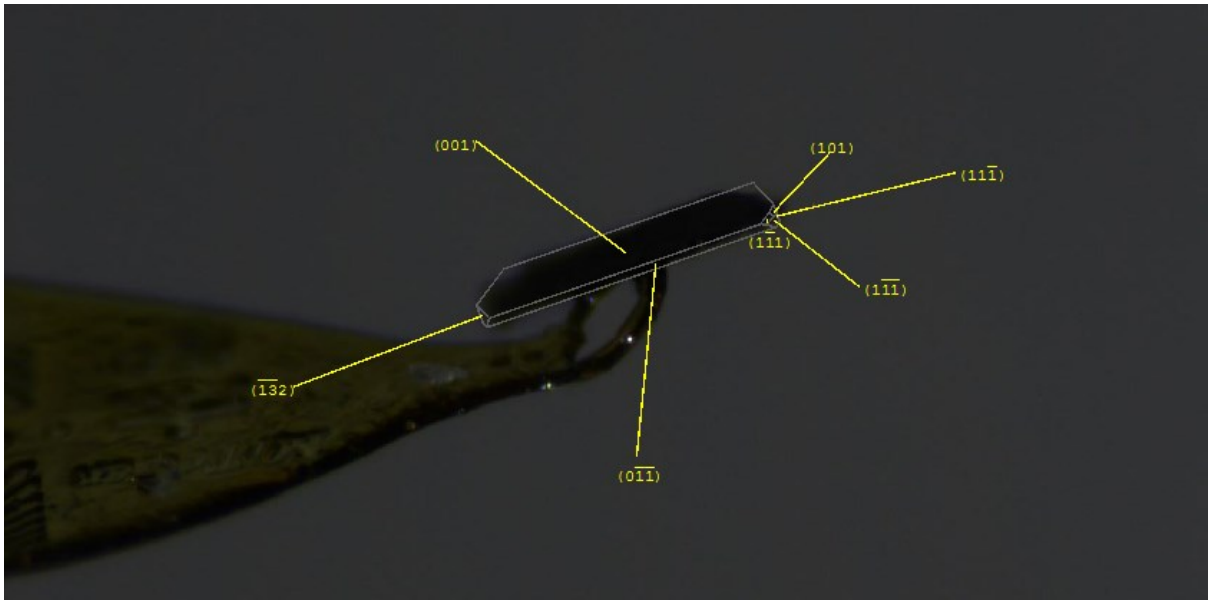

Figure S16. Crystal of (**azu**)$_3$(**ofiab**)$_2$ with most pronounced crystal faces indexed.

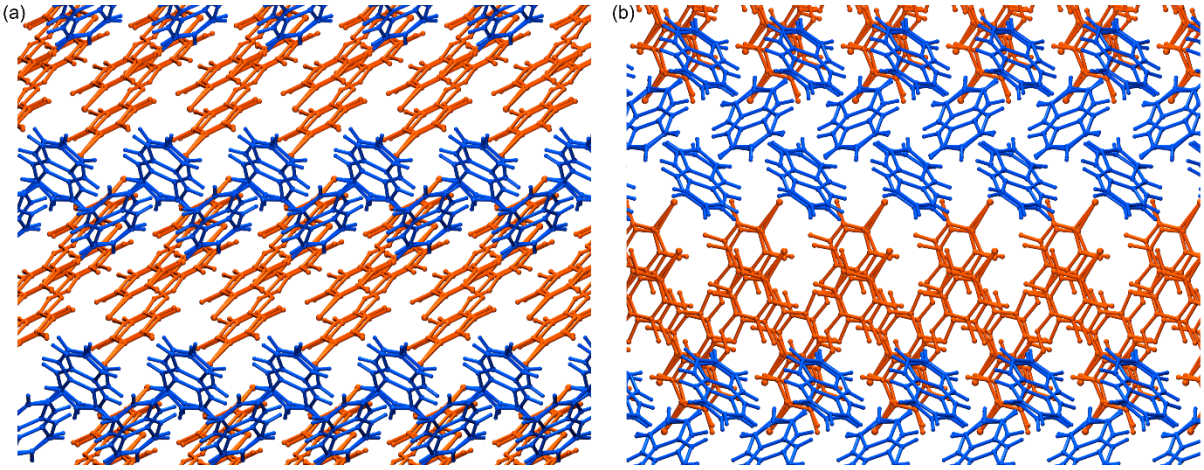

Figure S17. Two views of the crystal structure of (**azu**)$_3$(**ofiab**)$_2$ perpendicular to the crystallographic planes (a) (001) and (b) (011). Note that, while all **ofiab** moities are parallel, there are two groups of differently oriented **azu** molecules.

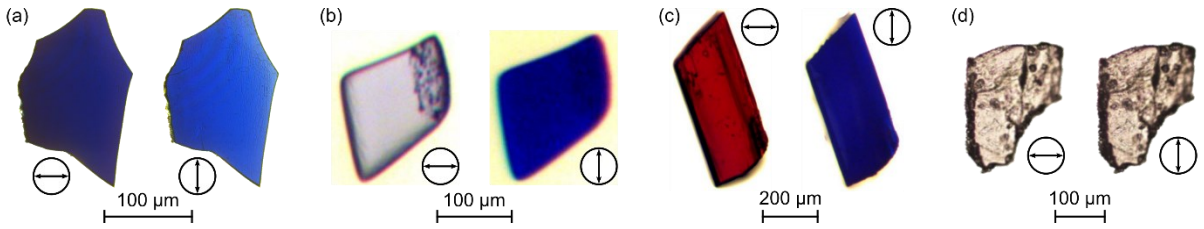

Figure S18. Additional photographs showing the (a) weak dichroism of **azu**,on the (100) face, (b) dichroism of (**azu**)$_2$(**14tfib**)$_3$, (c) pleochroism of (**azu**)(**ofiab**)$_2$, and (d) no observable dichroism in the case of (**nap**)(**14tfib**)$_2$.

5. Computational details

Starting from the experimentally obtained crystal structure *exp*-(**azu**)$_2$(**14tfib**)$_3$, two hypothetical structures were generated: *inv*-(**azu**)$_2$(**14tfib**)$_3$ and *alt*-(**azu**)$_2$(**14tfib**)$_3$. In *inv*-(**azu**)$_2$(**14tfib**)$_3$, the orientation of the **azu** molecule was inverted around its centroid, keeping the $P\bar{1}$ space group of the original structure. For *alt*-(**azu**)$_2$(**14tfib**)$_3$, the inversion centre was removed, lowering the symmetry of the structure to *P*1 and doubling the asymmetric unit, which consequently contained two molecules of **azu**. One of these molecules was inverted around its centroid and the other one was left in original orientation, simulating a simple case of the 50:50 disorder of **azu**.

Three structure models were also generated for the putative cocrystal (**nap**)$_2$(**14tfib**)$_3$ through replacing **azu** in the experimentally obtained structure of (**azu**)$_2$(**14tfib**)$_3$ by a carefully fitted rigid-body model of **nap** (taken from CSD refcode NAPHTA31). Due to the difference in molecular symmetry of **azu** and **nap**, two different models ((**nap**)$_2$(**14tfib**)$_3$-$P\bar{1}$-1 and (**nap**)$_2$(**14tfib**)$_3$-$P\bar{1}$-2) were obtained with different orientations of **nap** relative to **azu** in the original structure (Fig. S16). Additionally, a structure model was created with the space group transformed from $P\bar{1}$ to *P*1 subgroup, where both orientations of **nap** (both "red" and "blue", Fig. S16) were included in an alternating fashion ((**nap**)$_2$(**14tfib**)$_3$-$P\bar{1}$-3).

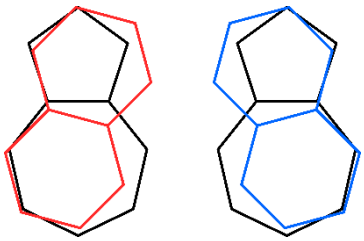

Figure S19. Two possible orientations of **nap** (in red or blue) in the putative structure models of (**nap**)$_2$(**14tfib**)$_3$ relative to the original position of **azu** (in black) in the experimentally determined structure of (**azu**)$_2$(**14tfib**)$_3$.

For (**azu**)(**14tfib**)$_2$, the disorder of **azu** around the crystallographic inversion centre precluded direct optimization of the experimentally obtained structure. A few different structure models were generated:

1) *par*-(**azu**)(**14tfib**)$_2$-111, where the original unit cell is preserved, the space group symmetry is lowered from $P\bar{1}$ to *P*1, and all the **azu** molecules are parallel, with their dipole moments also parallel;

2) *alt*-(**azu**)(**14tfib**)$_2$-112, *alt*-(**azu**)(**14tfib**)$_2$-121 and *alt*-(**azu**)(**14tfib**)$_2$-211, where the space group symmetry is lowered from $P\bar{1}$ to P1 and the unit cell is doubled into a 1×1×2, 1×2×1 or 2×1×1 supercell, respectively, with the orientations of the neighbouring **azu** molecules and their dipoles set as antiparallel, i.e. alternating along the ladder-like XB chain.

For the structure of **azu**, its disorder around an inversion centre again required more complicated structural models to be generated for optimization. Starting from a structure in space group $P2_1/a$ (CSD refcode AZLENE02), two structure models, **azu**-$P2_1$ and **azu**-*Pa* were generated by transforming it into two different subgroups, $P2_1$ and *Pa*, respectively. Moreover, a four-fold 1×2×2 supercell model (**azu**-*P*1-122) was also generated, corresponding to the most stable model reported by Dittrich et al.[11]

All structures were subjected to geometry optimization, with both the unit cell parameters and the atom positions allowed to vary, with the input files generated using the program cif2cell.[12] Periodic density functional theory (DFT) calculations were performed using CASTEP 19.11,[13] utilizing the Perdew-Burke-Ernzerhof (PBE)[14] generalized gradient approximation – GGA-type functional with the many-body dispersion (MBD*)[15–17] correction. Core electrons were described by ultrasoft pseudopotentials and the plane-wave basis set was truncated at 700 eV. Brillouin zone was sampled using a Monkhorst-Pack grid[18] with *k*-point spacing of 0.07 Å^{-1}. Sizes of the standard and fine fast Fourier transform grids were defined as 2 and 3 times of the diameter of the cut-off sphere, respectively. Convergence criteria were defined as follows: maximum energy change $2\cdot10^{-5}$ eV/atom, maximum force on atom $3\cdot10^{-2}$ eV Å^{-1}, maximum atom displacement 10^{-3} Å and maximum residual stress 10^{-1} GPa.

Only the most stable structure for each phase was used for the comparison of the halogen bond lengths between experimental and calculated structures and the calculation of the cocrystal formation energy.

Electron density distributions of **azu** and **nap** were calculated using Gaussian 16,[19] and the electrostatic potential (ESP) surfaces were plotted with VESTA.[20] The calculations utilized B3LYP functional and 6-311G(d,p) basis set. The ESP maps were plotted on 0.002 a.u. total electron density isosurfaces.

Table S2. Relative calculated energies of different structural models for **azu** and its cocrystals (**azu**)$_2$(**14tfib**)$_3$ and (**azu**)(**14tfib**)$_2$, with the lowest energy models highlighted in gray.

model	$\Delta E_{f,rel}$ (kJ/mol)
azu-$P2_1$-111	0.00
azu-*Pa*-111	2.52
azu-$P\bar{1}$-122	2.28

model	$\Delta E_{f,rel}$ (kJ/mol)
exp-(**azu**)$_2$(**14tfib**)$_3$	0.00
alt-(**azu**)$_2$(**14tfib**)$_3$	4.25
inv-(**azu**)$_2$(**14tfib**)$_3$	9.28

model	$\Delta E_{f,rel}$ (kJ/mol)
par-(**azu**)(**14tfib**)$_2$-111	2.09
alt-(**azu**)(**14tfib**)$_2$-112	0.51
alt-(**azu**)(**14tfib**)$_2$-121	2.56
alt-(**azu**)(**14tfib**)$_2$-211	0.00

Table S3. Relative calculated energies for different structures of the putative cocrystal (**nap**)$_2$(**14tfib**)$_3$, with the lowest energy model highlighted in gray.

	(**nap**)$_2$(**14tfib**)$_3$-$P\bar{1}$-1	(**nap**)$_2$(**14tfib**)$_3$-$P\bar{1}$-2	(**nap**)$_2$(**14tfib**)$_3$-$P1$-3
$\Delta E_{f,rel}$ (kJ/mol)	0.00	2.03	3.14

Table S4. Comparison of the experimental and calculated halogen bond lengths in the cocrystals (**azu**)$_2$(**14tfib**)$_3$, (**azu**)(**14tfib**)$_2$, (**nap**)$_2$(**14tfib**)$_3$ and (**nap**)(**14tfib**)$_2$.

(Co)crystal structure	**Experimental XB length, $d_{I\cdots plane}$ / Å**	**Calculated XB length, $d_{I\cdots plane}$ / Å**
(**azu**)$_2$(**14tfib**)$_3$@150 K	3.287; 3.316 (to 5-membered ring) 3.424 (to 7-membered ring)	3.103; 3.132 (to 5-membered ring) 3.357 (to 7-membered ring)
(**azu**)$_2$(**14tfib**)$_3$@253 K	3.307; 3.361 (to 5-membered ring) 3.436 (to 7-membered ring)	
(**azu**)(**14tfib**)$_2$@253 K	3.345; 3.411	3.101; 3.126; 3.178; 3.265 (to 5-membered ring) 3.161; 3.171; 3.274; 3.363 (to 7-membered ring)
"(**nap**)$_2$(**14tfib**)$_3$"	-	3.373; 3.514; 3.521
(**nap**)(**14tfib**)$_2$@RT (CSD NICTAW)	3.449; 3.470	3.229; 3.489
(**nap**)(**14tfib**)$_2$@110 K (CSD NICTAW01)	3.395; 3.432	

Table S5. Calculated formation energies for the cocrystals (**azu**)$_2$(**14tfib**)$_3$, (**azu**)(**14tfib**)$_2$, (**nap**)$_2$(**14tfib**)$_3$, (**nap**)(**14tfib**)$_2$.

Reaction	ΔE_f (kJ/mol)
2 **azu** + 3 **14tfib** → (**azu**)$_2$(**14tfib**)$_3$	−5.00
azu + 2 **14tfib** → (**azu**)(**14tfib**)$_2$	−4.10
2 **nap** + 3 **14tfib** → (**nap**)$_2$(**14tfib**)$_3$	+3.65
nap + 2 **14tfib** → (**nap**)(**14tfib**)$_2$	−1.32

6. TGA/DSC analysis

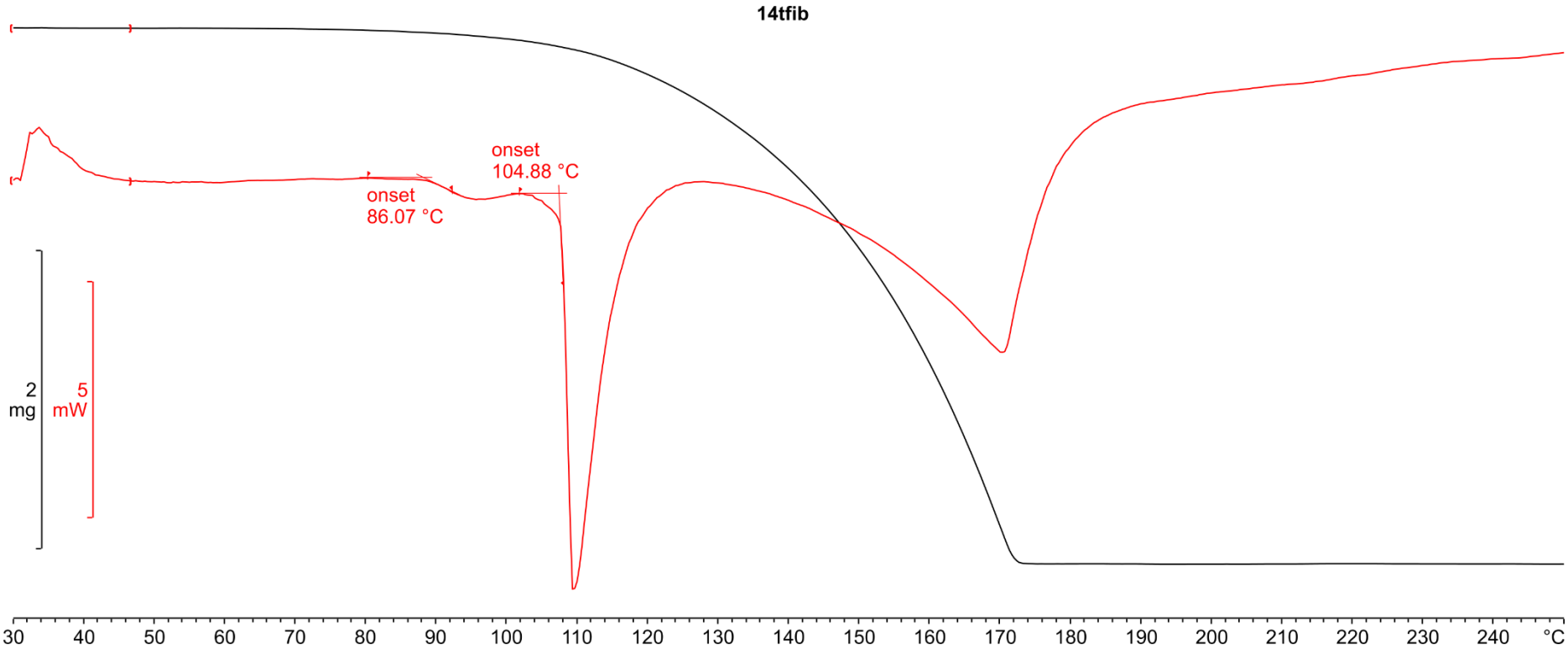

Figure S20. TGA (black) and DSC (red) curves for **14tfib**. The DSC curve shows a small peak (onset 86.07 °C) associated with the polymorphic transition from low-temperature to the high-temperature polymorph of **14tfib**,[21] with the larger peak (onset 104.88 °C) corresponding to the melting of **14tfib**.

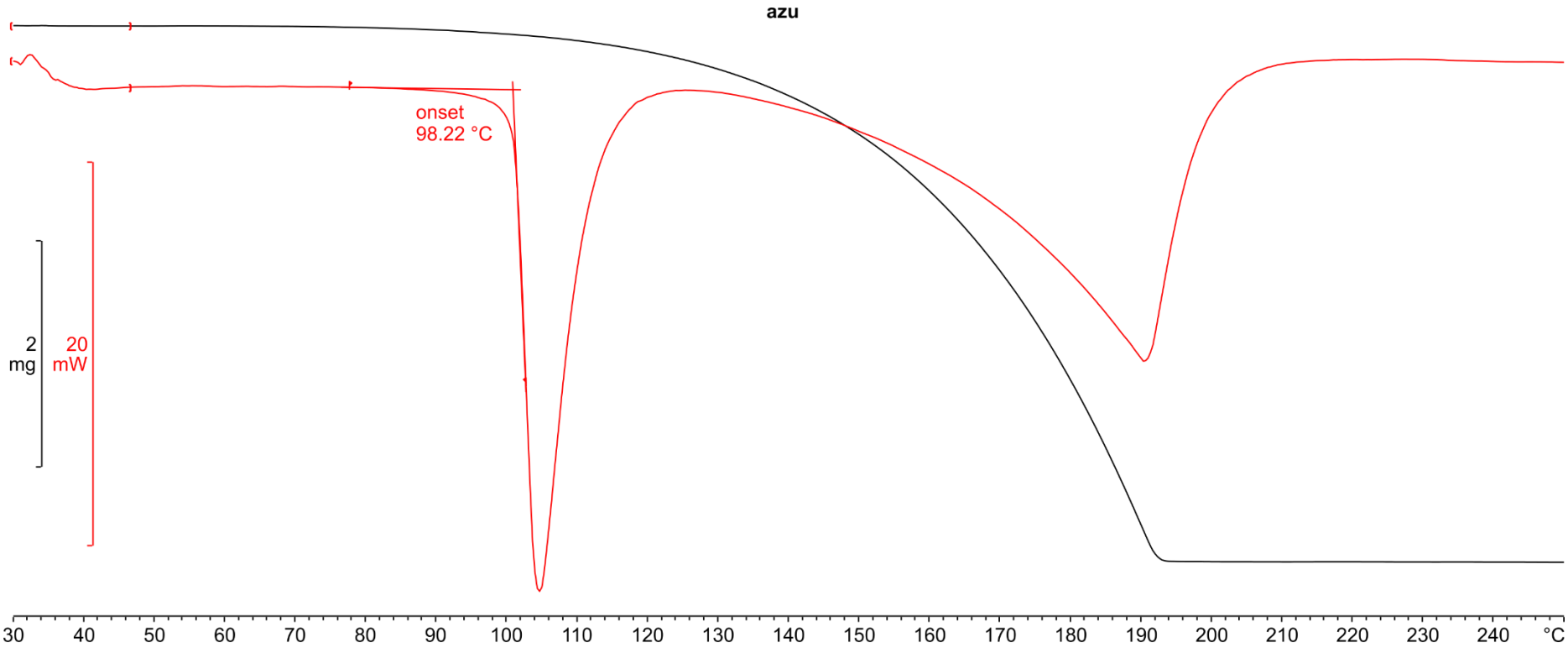

Figure S21. TGA (black) and DSC (red) curves for **azu**. The DSC curve shows a large peak (onset 98.22 °C) corresponding to the melting of **azu**.

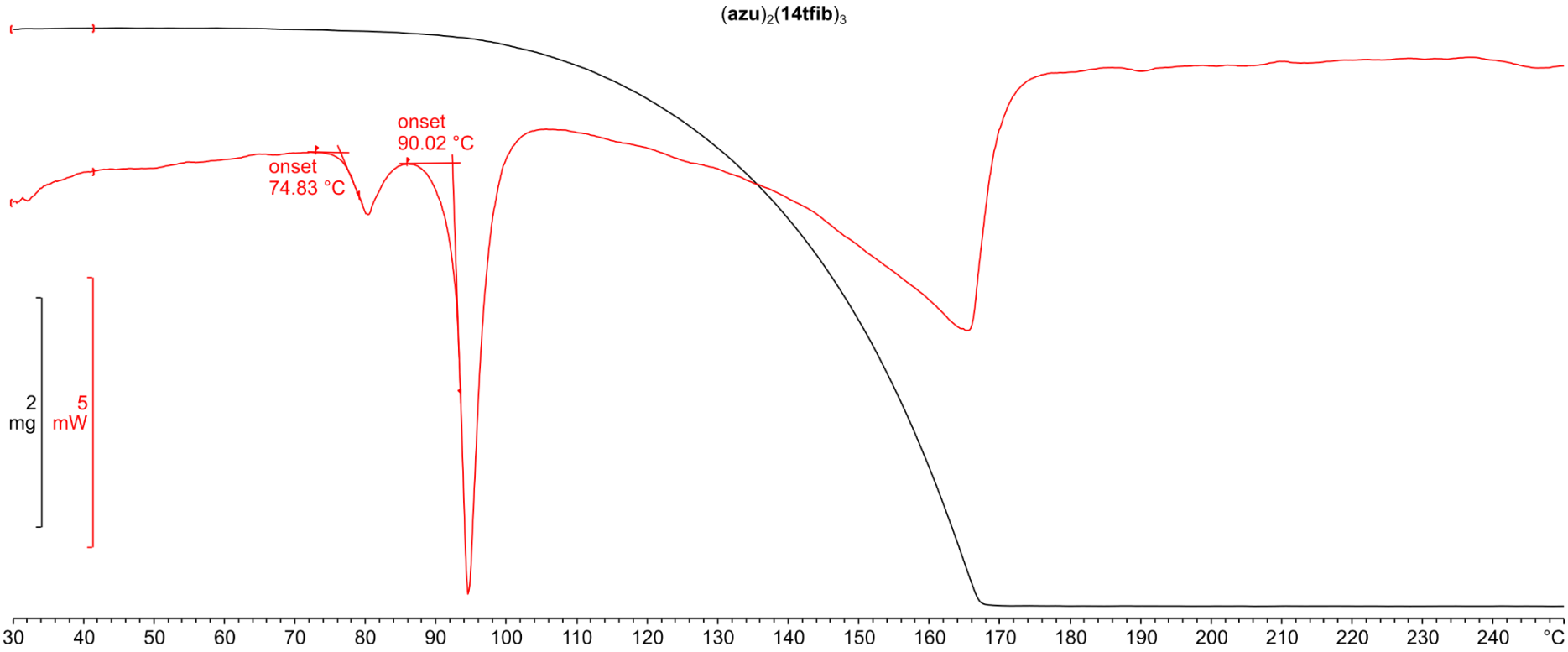

Figure S22. TGA (black) and DSC (red) curves for (**azu**)$_2$(**14tfib**)$_3$. The DSC curve shows a small peak (onset 74.83 °C) presumably due to the polymorphic transition of (**azu**)$_2$(**14tfib**)$_3$, with the larger peak (onset 90.02 °C) corresponding to the melting of (**azu**)$_2$(**14tfib**)$_3$.

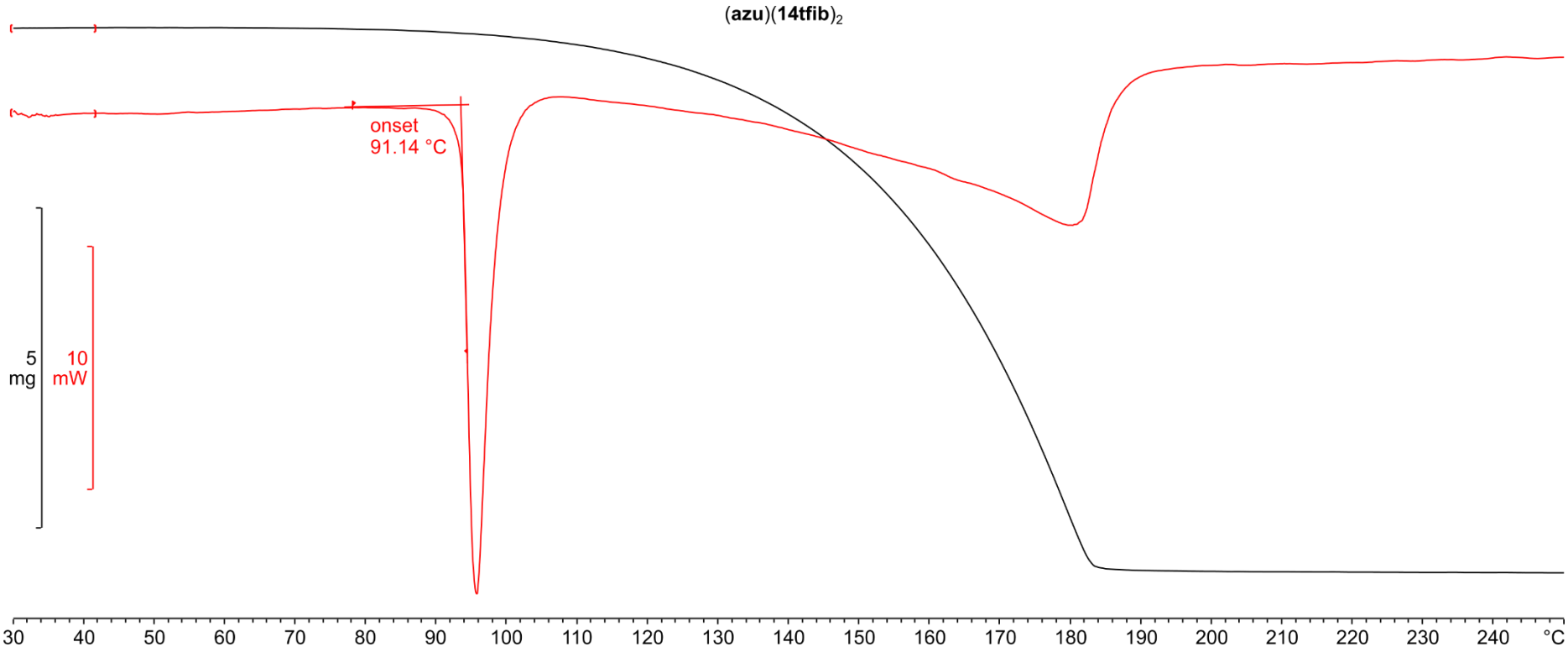

Figure S23. TGA (black) and DSC (red) curves for (**azu**)(**14tfib**)$_2$. The DSC curve shows a large peak (onset 91.14 °C) corresponding to the melting of (**azu**)(**14tfib**)$_2$.

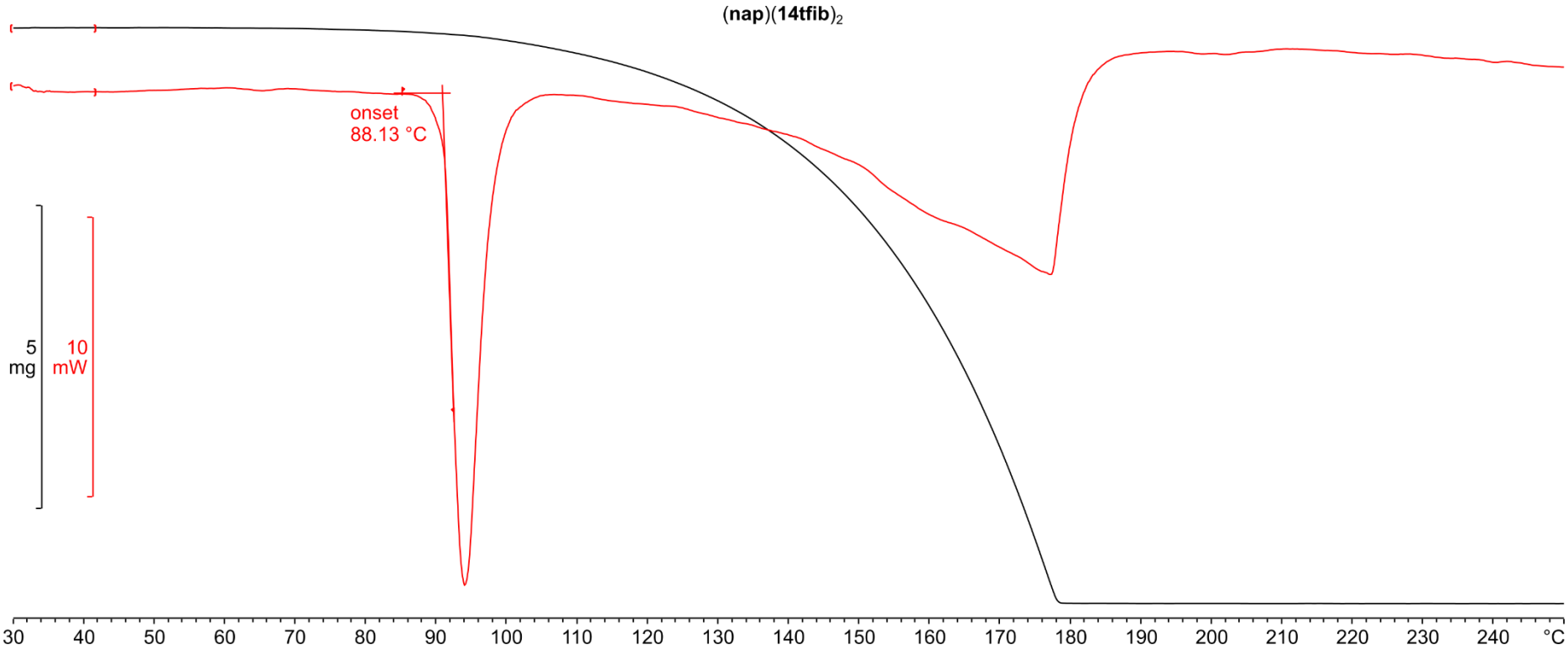

Figure S24. TGA (black) and DSC (red) curves for (**nap**)(**14tfib**)$_2$. The DSC curve shows a large peak (onset 88.13 °C) corresponding to the melting of (**nap**)(**14tfib**)$_2$.

7. Infrared spectra

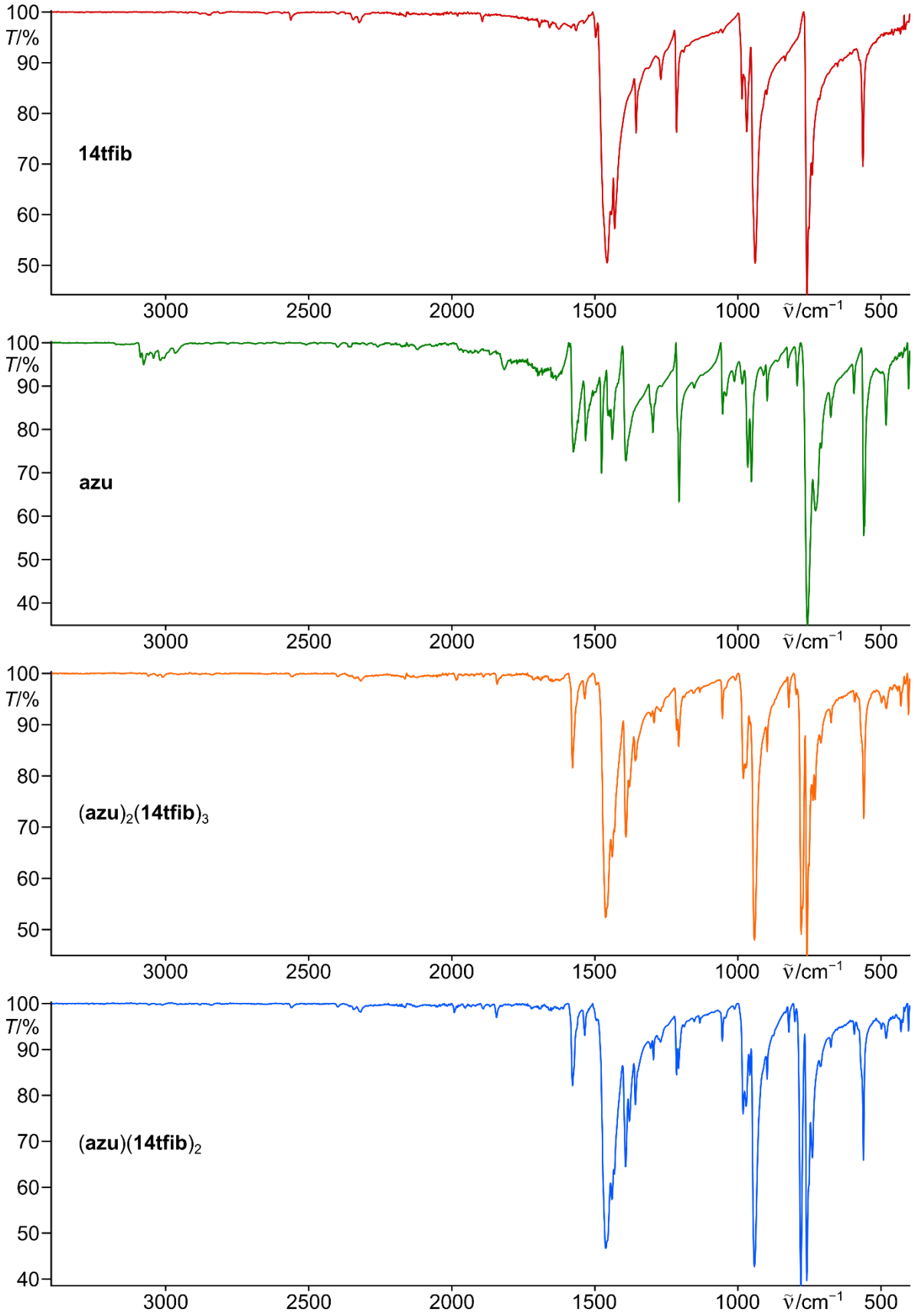

Figure S25. From top to bottom, ATR FTIR spectra of **14tfib**, **azu**, (**azu**)$_2$(**14tfib**)$_3$, (**azu**)(**14tfib**)$_2$.

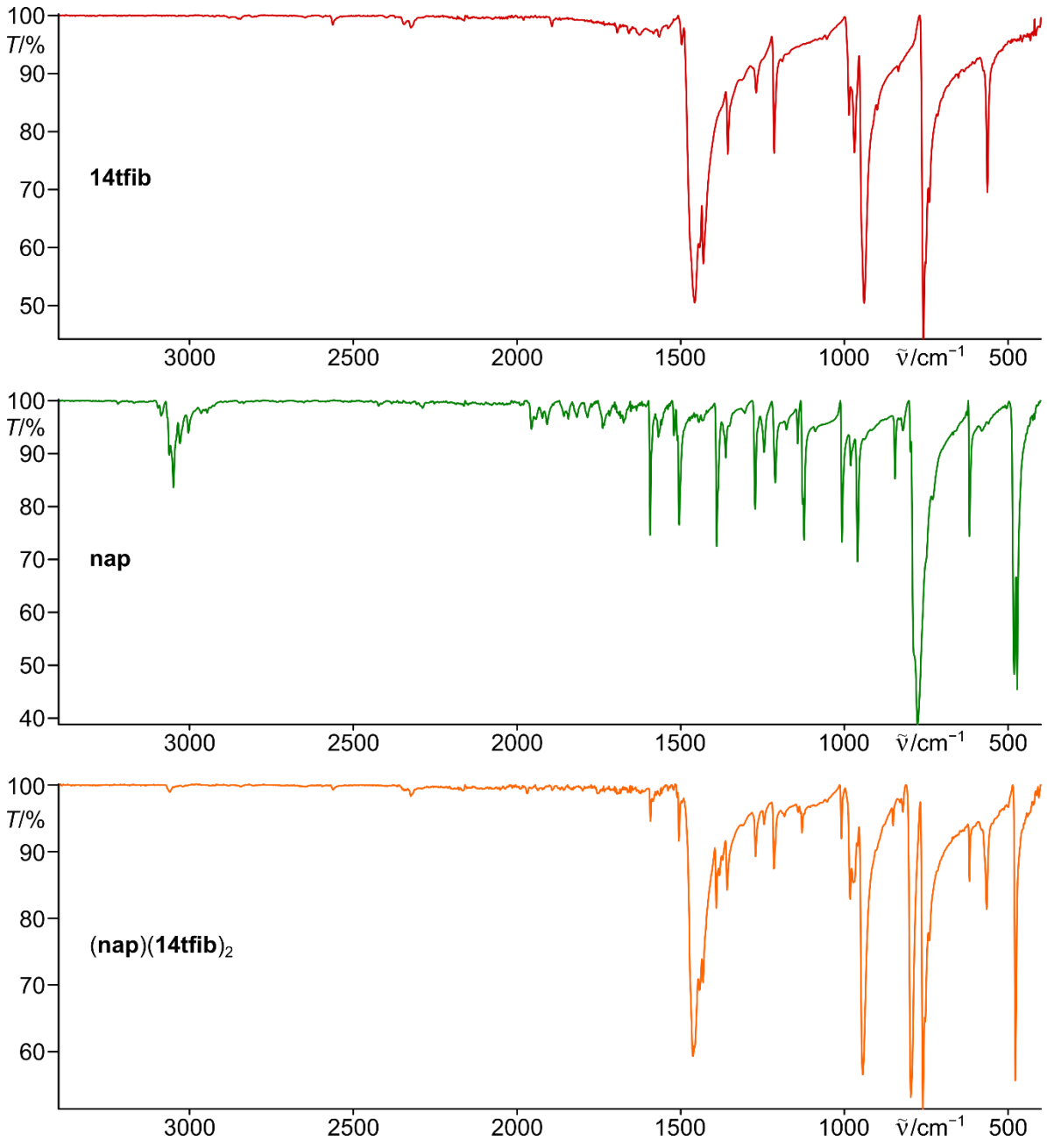

Figure S26. From top to bottom, ATR FTIR spectra of **14tfib**, **nap**, and (**nap**)(**14tfib**)$_2$.

8. References

1 O. S. Bushuyev, A. Tomberg, T. Friščić and C. J. Barrett, *J. Am. Chem. Soc.*, 2013, **135**, 12556.
2 *STARe Evaluation Software*, Mettler-Toledo GmbH, 1993.
3 Bruker, *APEX3*, Bruker AXS Inc., Madison, Wisconsin, USA, 2012.
4 L. Krause, R. Herbst-Irmer, G. M. Sheldrick and D. Stalke, *J. Appl. Cryst.*, 2015, **48**, 3.
5 G. M. Sheldrick, *Acta. Cryst.*, 2015, **A71**, 3.
6 G. M. Sheldrick, *Acta. Cryst.*, 2015, **C71**, 3.
7 O. V. Dolomanov, L. J. Bourhis, R. J. Gildea, J. A. K. Howard and H. Puschmann, *J. Appl. Cryst.*, 2009, **42**, 339.
8 L. J. Farrugia, *J. Appl. Cryst.*, 2012, **45**, 849.
9 C. F. Macrae, I. Sovago, S. J. Cottrell, P. T. A. Galek, P. McCabe, E. Pidcock, M. Platings, G. P. Shields, J. S. Stevens, M. Towler and P. A. Wood, *J. Appl. Cryst.*, 2020, **53**, 226.
10 Persistence of Vision Pty. Ltd., *Persistence of Vision Raytracer*, Persistence of Vision Pty. Ltd., Williamstown, Victoria, Australia, 2018.
11 B. Dittrich, F. P. A. Fabbiani, J. Henn, M. U. Schmidt, P. Macchi, K. Meindl and M. A. Spackman, *Acta Cryst.*, 2018, **B74**, 416.
12 T. Björkman, *Comput. Phys. Commun.*, 2011, **182**, 1183.
13 S. J. Clark, M. D. Segall, C. J. Pickard, P. J. Hasnip, M. I. J. Probert, K. Refson and M. C. Payne, *Z. Kristallogr.*, 2005, **220**, 567.
14 J. P. Perdew, K. Burke and M. Ernzerhof, *Phys. Rev. Lett.*, 1996, **77**, 3865.
15 A. Tkatchenko, R. A. DiStasio, R. Car and M. Scheffler, *Phys. Rev. Lett.*, 2012, **108**, 236402.
16 A. Ambrosetti, A. M. Reilly, R. A. DiStasio and A. Tkatchenko, *J. Chem. Phys.*, 2014, **140**, 18A508.
17 A. M. Reilly and A. Tkatchenko, *Chem. Sci.*, 2015, **6**, 3289.
18 H. J. Monkhorst and J. D. Pack, *Phys. Rev. B*, 1976, **13**, 5188.
19 M. J. Frisch, G. W. Trucks, H. B. Schlegel, G. E. Scuseria, M. A. Robb, J. R. Cheeseman, G. Scalmani, V. Barone, G. A. Petersson, H. Nakatsuji, X. Li, M. Caricato, A. V. Marenich, J. Bloino, B. G. Janesko, R. Gomperts, B. Mennucci, H. P. Hratchian, J. V. Ortiz, A. F. Izmaylov, J. L. Sonnenberg, D. Williams-Young, F. Ding, F. Lipparini, F. Egidi, J. Goings, B. Peng, A. Petrone, T. Henderson, D. Ranasinghe, V. G. Zakrzewski, J. Gao, N. Rega, G. Zheng, W. Liang, M. Hada, M. Ehara, K. Toyota, R. Fukuda, J. Hasegawa, M. Ishida, T. Nakajima, Y. Honda, O. Kitao, H. Nakai, T. Vreven, K. Throssell, J. A. Montgomery Jr., J. E. Peralta, F. Ogliaro, M. J. Bearpark, J. J. Heyd, E. N. Brothers, K. N. Kudin, V. N. Staroverov, T. A. Keith, R. Kobayashi, J. Normand, K. Raghavachari, A. P. Rendell, J. C. Burant, S. S. Iyengar, J. Tomasi, M. Cossi, J. M. Millam, M. Klene, C. Adamo, R. Cammi, J. W. Ochterski, R. L. Martin, K. Morokuma, O. Farkas, J. B. Foresman and D. J. Fox, *Gaussian 16 Revision B.01*, 2016.
20 K. Momma and F. Izumi, *J. Appl. Cryst.*, 2011, **44**, 1272.
21 G. S. Pawley, G. A. Mackenzie and O. W. Dietrich, *Acta Cryst.*, 1977, **A33**, 142.